CHINESE OPTICS LETTERS

Vol. 19, No. 7 | July 2021

Recent advance in hollow-core fiber high-temperature and high-pressure sensing technology [Invited]

Zhe Zhang (张 哲)[1,2], Yingying Wang (汪滢莹)[1], Min Zhou (周 敏)[2], Jun He (何 俊)[2*], Changrui Liao (廖常锐)[2], and Yiping Wang (王义平)[2]

[1] Guangdong Provincial Key Laboratory of Optical Fiber Sensing and Communication, Institute of Photonics Technology, Jinan University, Guangzhou 511443, China

[2] Key Laboratory of Optoelectronic Devices and Systems of Ministry of Education/Guangdong Province, College of Physics and Optoelectronic Engineering, Shenzhen University, Shenzhen 518060, China

*Corresponding author: hejun07@szu.edu.cn

Received April 8, 2021 | Accepted May 25, 2021 | Posted Online July 20, 2021

The pure-silica hollow-core fiber (HCF) has excellent thermostabilities that can benefit a lot of high-temperature sensing applications. The air-core microstructure of the HCF provides an inherent gas container, which can be a good candidate for gas or gas pressure sensing. This paper reviews our continuous efforts to design, fabricate, and characterize the high-temperature and high-pressure sensors with HCFs, aiming at improving the sensing performances such as dynamic range, sensitivity, and linearity. With the breakthrough advances in novel anti-resonant HCFs, sensing of high temperature and high pressure with HCFs will continuously progress and find increasing applications.

Keywords: hollow-core fiber; high-temperature sensing; high-pressure sensing.
DOI: 10.3788/COL202119.070601

1. Introduction

Measurement of high temperature and high pressure is of great significance in modern industries such as aerospace, chemical industry, deep-water exploration, and petroleum drilling. Since the 1970s, optical fiber sensing technology has become tremendously successful owing to its high integration, immunity to electromagnetic interference, resistance to harsh environments, as well as capability of networking and distributed sensing[1–8]. In terms of high-temperature sensing, a variety of fiber-optic sensors such as ultrafast laser-induced fiber Bragg gratings (FBGs)[9–14], sapphire FBGs[15–21], long-period fiber gratings inscribed by a CO_2 laser[22–24] or arc discharge[25–27], fiber Mach–Zehnder interferometers (MZIs)[28–31], and fiber Fabry–Perot interferometers (FPIs)[32–38] have been well developed in the past decades. Sapphire fibers can withstand a temperature higher than 1800°C, where the main drawbacks are the poor mechanical and modal properties, as well as the expensive price. As a result, sapphire fiber high-temperature sensors are destined to be used merely in certain occasions such as aerospace or military industries. In contrast, conventional single-, few-, or multi-mode silica fibers are the most common bases for high-temperature sensors. However, conventional silica fibers suffer from poor linearity and stability in high-temperature environments before annealing treatments, which can be attributed to the different thermo-expansion coefficients between the fiber cladding (silica) and Ge-doped silica core, rendering the release of residual stress when the fiber is heated to the material softening temperature[39–43]. As a result, the isothermal annealing treatment is necessary to eliminate the residual stress and improve the sensor's linearity and stability before using.

Hollow-core fibers (HCFs) guide light in the air core and can be classified into two categories: photonic bandgap (PBG) and anti-resonant reflection (ARR) HCFs according to the light confinement mechanism. Among the ARR-HCFs, hollow silica capillaries can be considered as the most original HCF, which exhibits large loss and thus is limited to the ultrashort-distance transmission. Typically, HCFs are drawn from pure-silica capillaries[44–53], which can reduce the residual stress within the fiber effectively owing to the single material construction (i.e., the same thermo-expansion coefficient). As such, HCF-based high-temperature sensors may withstand a higher temperature and linearity. In addition, the air-core microstructure of HCF provides an inherent gas container[54–59], which can be a good candidate for gas or gas pressure sensing[60–65]. Holey microstructures can also provide extra degrees of freedom for geometry modification through post-thermal treatment or selective filling of the air holes. The confinement of gas and optical guided modes simultaneously within the hollow core allows strong light/gas interaction over an extended length and may be a good candidate for highly sensitive gas sensors or lasers[66–73].

This paper reviews our works over the past five years, which focused on the design, preparation, and characterization of the HCF microcavity high-temperature and high-pressure sensors. Section 2 describes the high-temperature sensors based on HCF MZIs and fiber-tip FPIs, respectively. Section 3 includes the HCF high-pressure sensors with wavelength and phase demodulation approaches, respectively. In Section 4, a dual-cavity FPI sensor for simultaneous measurement of high temperature and high pressure is detailed. A brief conclusion and prospects of the HCF-based high-temperature and high-pressure sensing technology are discussed in Section 5.

2. HCF High-Temperature Sensors

Optical fiber microcavity MZIs or FPIs have been widely adopted for temperature sensing, which shows advantages of compactness, high sensitivity, and low costs. Tapering, arc discharge, and ultrafast laser micromachining are typical approaches for creating microcavities in conventional solid-core fibers. However, the microcavity quality and preparation repeatability are crucially limited by the processing technique. Moreover, repeated adiabatic annealing is necessary for the sensor to release the residual stress and improve the linearity of the sensor. Instead, HCFs provide a natural high-quality microcavity, which does not only improve the preparation repeatability but renders a higher working temperature and linearity.

2.1. MZI high-temperature sensor

The MZI high-temperature sensor can be simply constructed by sandwiching a short piece of HCF between two single-mode fibers (SMFs) with precious slicing and optimized arc discharge techniques[31]. The sensor structure is schematically illustrated in Fig. 1(a), where the two splicing points between the HCF and SMF act as the beam splitter and combiner, respectively, and the air core and silica cladding of the HCF act as the two arms of the MZI. For a higher fringe visibility, a little offset is introduced in the second splicing joint, i.e., the beam combiner. Figure 1(b) shows the simulation results of beam transmission through the proposed MZI, which clearly depicts the beam splitting and combining behaviors. Since the optical path difference (OPD) is created between the core and cladding beams, the white-light interference spectrum can be obtained. The transmission intensity can be expressed as

$$I = I_{\mathrm{co}} + I_{\mathrm{cl}} + 2\sqrt{I_{\mathrm{co}} I_{\mathrm{cl}}}\cos\left(\frac{2\pi L\Delta n}{\lambda} + \varphi_0\right), \tag{1}$$

where λ and L are the wavelength of light and the length of the HCF, respectively. $\Delta n = n_{\mathrm{cl}}^{\mathrm{eff}}(T) - n_{\mathrm{co}}^{\mathrm{eff}}(T)$ is the effective refractive index (RI) difference between the two interference beams, $n_{\mathrm{cl}}^{\mathrm{eff}}(T)$ and $n_{\mathrm{co}}^{\mathrm{eff}}(T)$ denote the effective RIs of the cladding and core beams, respectively, and φ_0 is the initial phase of interference. As such, the wavelength of the mth-order interference minimum can be calculated to be

$$\lambda_m = \frac{2\pi L\Delta n}{(2m+1)\pi - \varphi_0}. \tag{2}$$

The thermo-optic and thermo-expansion coefficients differences between silica and air will result in the change of Δn and L, respectively, with temperature variation. According to Eq. (2), λ_m will shift to longer wavelengths with rising temperatures. By making differentiation for Eq. (2), the temperature sensitivity can be expressed by

$$\frac{\mathrm{d}\lambda}{\mathrm{d}T} = \lambda\left\{\frac{1}{n_{\mathrm{si}}^{\mathrm{eff}}(T) - n_{\mathrm{air}}^{\mathrm{eff}}(T)}\left[\frac{\mathrm{d}n_{\mathrm{si}}^{\mathrm{eff}}(T)}{\mathrm{d}T} - \frac{\mathrm{d}n_{\mathrm{air}}^{\mathrm{eff}}(T)}{\mathrm{d}T}\right] + \alpha\right\}, \tag{3}$$

where α and $\mathrm{d}n_{\mathrm{si}}^{\mathrm{eff}}(T)/\mathrm{d}T$ represent the thermal-expansion and thermo-optic coefficient of silica, respectively, and $\mathrm{d}n_{\mathrm{air}}^{\mathrm{eff}}(T)/\mathrm{d}T$ denotes the RI change of air with temperature. The thermo-optic coefficient of fused silica at different temperatures and wavelength ranges can be obtained from Ref. [74], which is illustrated in Table 1.

The thermal-expansion coefficient of fused silica[75] is $\sim 0.55 \times 10^{-6}\ ^{\circ}\mathrm{C}^{-1}$, which is far less than its thermo-optic coefficient ($> 10^{-5}$). As such, α can be neglected in some occasions. By optimizing the arc discharge parameters, sensor samples with different offset distance d are prepared, the transmission spectra

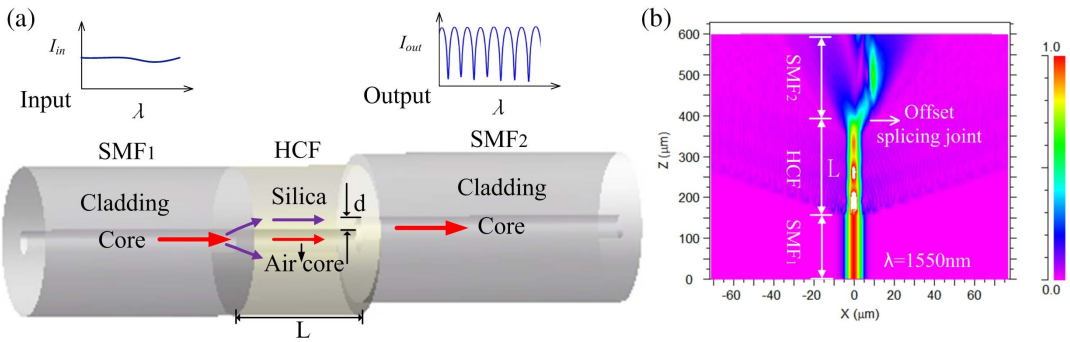

Fig. 1. (a) Schematic diagram of the proposed SMF-HCF-SMF temperature sensor; (b) simulation result of light propagation in the SMF-HCF-SMF configuration at 1550 nm.

Table 1. Refractive Index of Fused Silica versus Temperature[74].

λ (μm)	n (26°C)	n (471°C)	dn/dT (10^{-6} °C^{-1})	n (828°C)	dn/dT (10^{-6} °C^{-1})
0.57800	1.45899	1.46429	+11.9	1.46870	+12.1
1.12866	1.44903	1.45426	+11.8	1.45820	+11.4
1.36728	1.44635	1.45140	+11.4	1.45549	+11.4
1.52925	1.44444	1.44961	+11.6	1.45352	+11.3
1.66000	1.44307	1.44799	+11.1	1.45174	+10.8

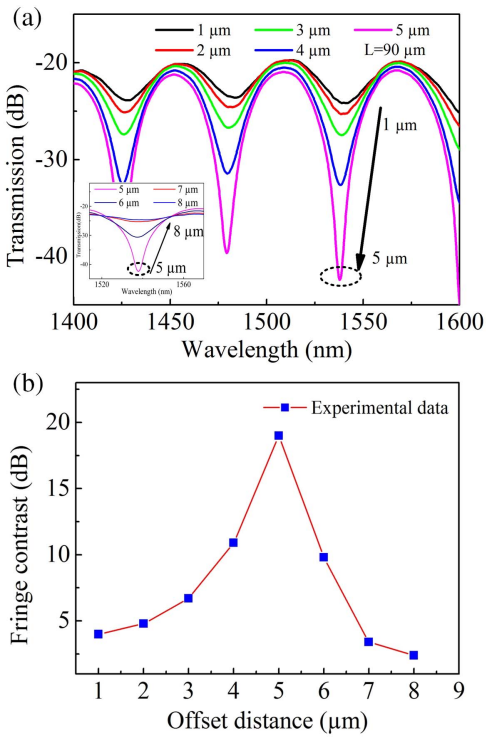

Fig. 2. (a) Transmission spectra for different offset distances; inset: transmission spectrum shrinking; (b) fringe contrast versus offset distance.

of which are shown in Fig. 2, where we can see that ~5 μm is the optimized offset distance (interference visibility > 20 dB). The geometry of one sensor sample is characterized by an optical microscope, as shown in Fig. 3(a), while Fig. 3(b) shows the microscope image of the employed HCF. Mode field distribution of the beam (at 1550 nm) after transmitting through a 90 μm long HCF is also measured by an infrared CCD, as shown in Fig. 3(c), where the cladding and core beams can be identified.

High-temperature tests are subsequently carried out by employing a high-temperature oven that can reach 1200°C with an accuracy of ±1°C. The interference dip positioned around 1375 nm is tracked with the changing temperature. The oven temperature is increased from 200°C to 900°C with a step of 100°C and kept for ~30 min at each step to obtain a stable spectrum. A clear "redshift" of the tracked dip is observed, as shown in Fig. 4(a). No obvious spectrum deterioration is observed, and only a wavelength shift of 1.4 nm is identified [Fig. 4(b)] when keeping the sensor at 900°C for 26 h. The phenomenon is beyond our expectation, since it implies that the residual stress is released. However, it is not hard to understand the origin of residual stress, which is believed to be introduced by the extrusions of fiber end facets during the fusion splicing processes. This adverse impact can be eliminated effectively by an improved fiber-tip FPI sensor structure, which will be detailed in the next section. The temperature is then decreased back to 200°C with a step of 100°C, and the spectral evolution is shown in Fig. 4(c). It is worth noting that the spectrum of Fig. 4(c) seems to include higher-order terms of interference, which is slightly different from Fig. 4(a). Preliminary analysis suggests that the RI profile of HCF cladding may be modified by the release of residual stress, and new cladding modes in the HCF may be excited. This frustrated effect can be removed by an improved fiber-tip FPI sensor, which is detailed in Section 2.2. The dip wavelength versus temperature in both heating and cooling processes is illustrated in Fig. 5(a), respectively. After repeating the heating and cooling cycles three times over 2 days, the tracked dip shows no divergency between heating and cooling processes, as shown in Fig. 5(b). The linear fitting yields a high correlation coefficient $R^2 = 0.9994$, and a high-temperature sensitivity of 41 pm/°C.

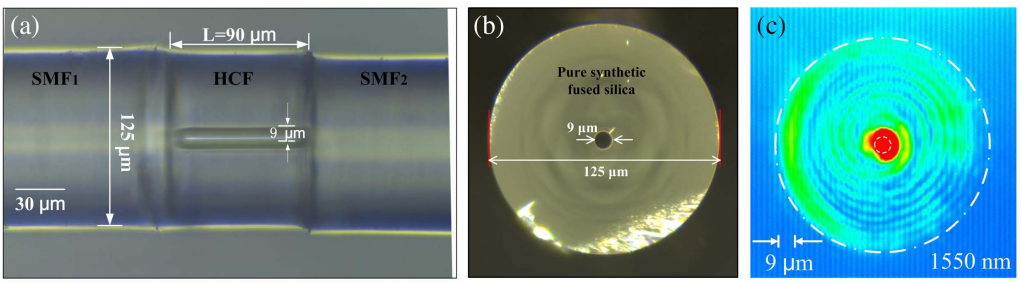

Fig. 3. (a) Side view of the sensing head; (b) cross section of the HCF; (c) near field image at the end facet of a 90 μm HCF with the other end facet aligned to the lead-in SMF_1.

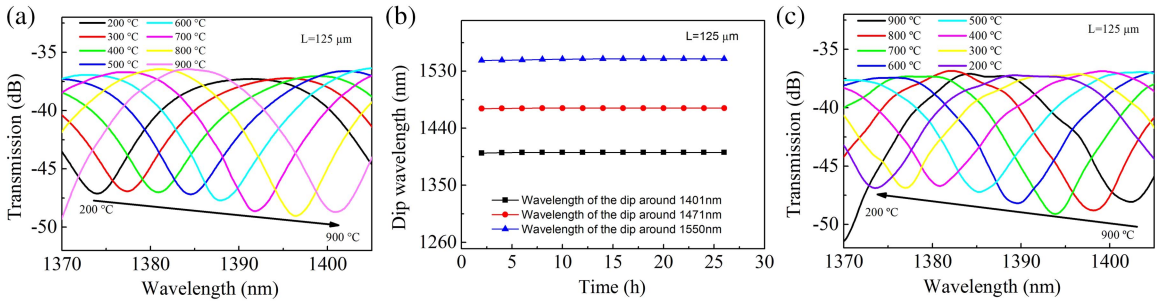

Fig. 4. (a) Transmission spectrum evolution from 200°C to 900°C; (b) wavelength of the interference minimum around 1401, 1471, and 1550 nm versus heating time at 900°C, respectively; (c) transmission spectrum evolution from 900°C to 200°C.

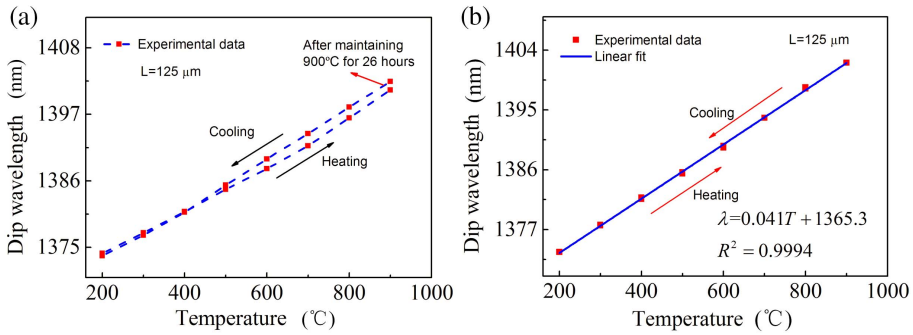

Fig. 5. Dip wavelength versus temperature in both heating and cooling processes (a) before and (b) after three cycles of annealing.

2.2. Annealing-free fiber-tip FPI high-temperature sensor

To eliminate the adverse impact of residual stress as well as high-order modes distraction, we propose an annealing-free HCF-tip FPI high-temperature (1100°C) sensor[38]. This sensor schema exhibits an excellent thermal stability and linearity ($R^2 > 0.99$ in the 100°C–1100°C range) even without the need for high-temperature annealing. The proposed sensor is schematically illustrated in Fig. 6(a), which is prepared by fusion splicing, followed by a precious cutting of the HCF with the assistance of a homemade microscope. As shown in Fig. 1, part of the light propagating in the lead-in SMF will be partially reflected at interface I due to the smaller core of the HCF than of the lead-in SMF, while part of the light will transmit into the silica cladding of the HCF. Light transmitted in the silica cladding will be partially reflected at interface II and transmitted back into the lead-in SMF. It is worth noting that only the silica/air interfaces are considered as reflectors, since the RI difference between the SMF core (Ge-doped silica) and the HCF cladding (pure silica) is too small. We define a parameter of γ to represent the proportion of light that suffers Fresnel reflection at interface I. As such, the reflective intensity at interface I can be written as

$$I_1 = I_0 \gamma R_1, \tag{4}$$

where I_0, γ, and R_1 denote the intensity of the incident light, the proportion of light that suffers Fresnel reflection at interface I, and the reflectivity of interface I, respectively. After transmitting in the cladding of the HCF for a length of L, the light is partially reflected at interface II, recoupling back into the lead-in SMF. The reflection intensity can be represented by

$$I_2 = I_0(1-\gamma)R_2, \tag{5}$$

where R_2 represents the reflectivity of interface II. Here, the transmission loss of HCF cladding is neglected since the HCF is short in length. It should be noted that the intensity ratio γ is determined by the air-core diameter of the HCF, since the mode field diameter of the lead-in SMF is fixed. To be specific, the mode field of the lead-in SMF is a Gaussian distribution with a diameter of ~10 μm, and vice versa, a smaller air core renders a smaller γ. As a result, the fringe visibility of the FPI, which is determined by the intensity ratio (I_1/I_2) of the two reflection

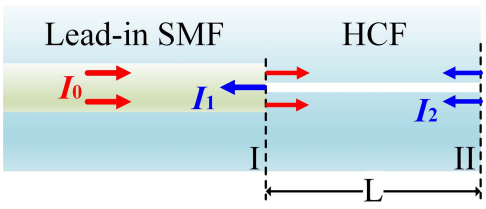

Fig. 6. Schematic illustration of the proposed FPI sensor. FPI, Fabry–Perot interferometer; SMF, single-mode fiber; I_1/I_2, intensity ratio; I_0, the intensity of the incident light; HCF, hollow-core fiber; L, length of HCF; interface I, the SMF end facet; interface II, the HCF end facet.

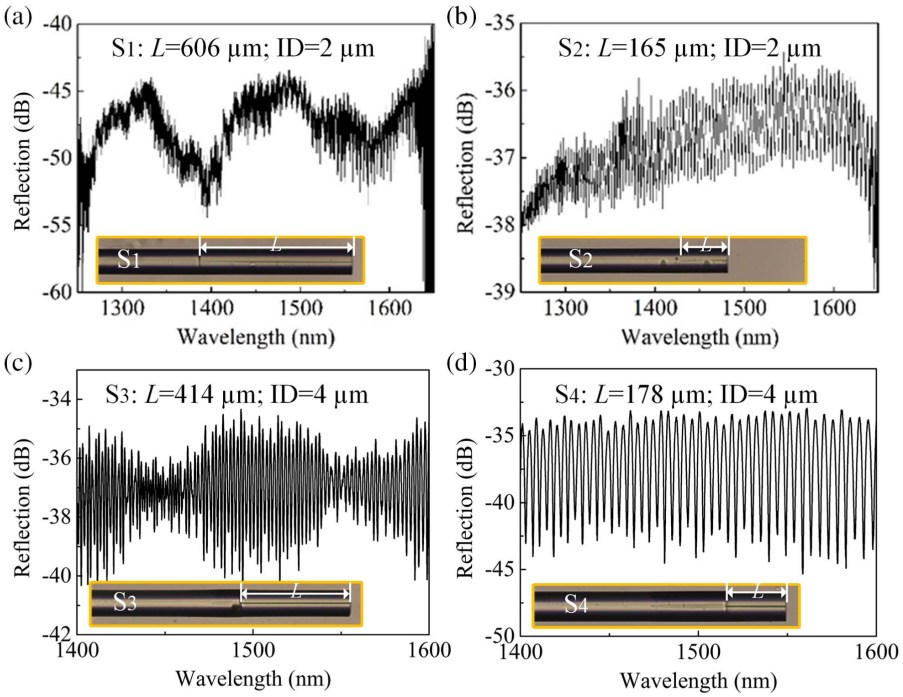

Fig. 7. Reflection spectra of the prepared FPIs with different HCF parameters.

beams, can be altered flexibly by changing the inner diameter (ID) of the HCF. However, the HCF with an ID larger than the core diameter of the lead-in SMF will result in a poor fringe visibility (< 2 dB), as reported in Ref. [76]. A poor fringe visibility will impose difficulties for peak tracking and the following demodulations. Figure 7 exhibits the reflection spectra of four prepared FPI sensor samples (S_1–S_4) with HCF IDs of 2 μm (S_1 and S_2) and 4 μm (S_3 and S_4), respectively. Sensor samples with an HCF ID of 4 μm show higher fringe visibility. As a result, the HCF with the 4 μm ID is chosen for the FPI sensor preparation.

In addition, the length L of the HCF affects the spectral quality of the FPI as well. Extra modes will be excited in the cladding of the HCF if the HCF is too long. The extra modes will result in a superimposed interference spectrum, as shown in Fig. 7(c), where a sample with a ~414 μm HCF renders a dense fringe modulated by a large envelope, implying multibeam interference. Figure 8(a) shows the "spectrum of spectrum" obtained by fast Fourier transform (FFT), where multiple frequencies can be identified. As such, the HCF length is vital for the spectrum quality, which is crucial for demodulation. By shortening the HCF to ~178 μm, a typical two-beam interference spectrum can be obtained and is shown in Fig. 7(d), and the FFT result is shown in Fig. 8(b).

High-temperature performance of the proposed fiber-tip FPI sensor is then experimentally studied, and the experimental equipment is the same as described above. Although the temperature sensitivity is wavelength dependent, while for simplicity and clarity purposes, we employ the interference dip at ~1550 nm as the temperature indicator. The wavelength of

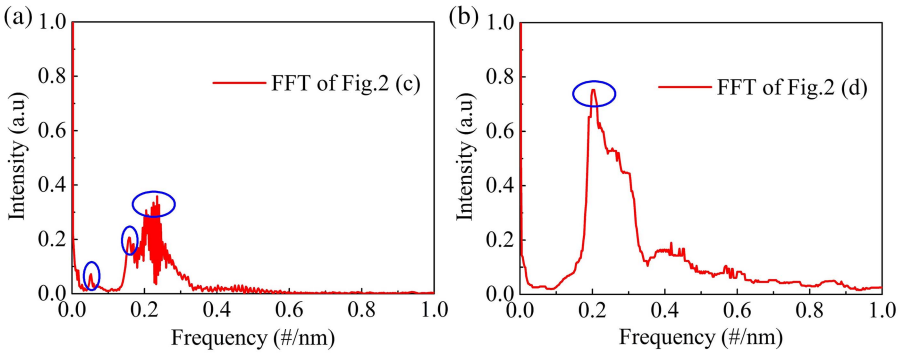

Fig. 8. Frequency spectra of the interference spectra of (a) S_3 and (b) S_4 obtained by fast Fourier transform (FFT).

the tracked dip presents a "redshift," with the temperature increasing, which is a combined result of the thermo-optic and thermal-expansion effects of silica. The temperature sensitivity can be expressed as

$$\frac{\mathrm{d}\lambda}{\mathrm{d}T}=\lambda\left[\frac{1}{n_{\mathrm{si}}^{\mathrm{eff}}(T)}\frac{\mathrm{d}n_{\mathrm{si}}^{\mathrm{eff}}(T)}{\mathrm{d}T}+\alpha\right], \tag{6}$$

where $\mathrm{d}n_{\mathrm{si}}^{\mathrm{eff}}(T)/\mathrm{d}T$ and α denote the thermo-optic and thermal-expansion coefficients of silica, respectively. Since $n_{\mathrm{si}}^{\mathrm{eff}}(T)$ increases with temperature, the contribution of the thermo-expansion effect cannot be neglected at high-temperature conditions according to Eq. (6). High-temperature tests within different temperature ranges are carried out, the results of which are depicted in Figs. 9(a)–9(f), respectively. No obvious thermal hysteresis and wavelength separation between the heating and cooling processes are observed, and the measurement linearities are all higher than 0.99 within each temperature range. Meanwhile, a ~0.2 nm wavelength separation between the heating and cooling processes is found when the temperature is increased to 900°C [Fig. 9(g)]. The small wavelength separation is believed to be the result of residual stress releasing, where a small amount of stress is introduced during the fusion splicing of the SMF and HCF. A repeated high-temperature test from 100°C to 900°C eliminates the wavelength separation effectively, and a high linearity of 0.997 is demonstrated [Fig. 9(h)]. Further on, we increase the temperature to 1000°C and 1100°C, respectively, where high linearities (> 0.99) without any thermal hysteresis are demonstrated [Figs. 9(i) and 9(j)] as well.

As such, the fiber-tip FPI sensor can work in a harsh environment of 1100°C with a high measurement linearity, which can be attributed to the excellent temperature performance of pure-silica HCFs. Meanwhile, the excellent high-temperature performance of the sensor before high-temperature annealing also confirms our conjecture that the HCF high-temperature sensor could dismiss the complicated isothermal annealing processes effectively. Linear fittings yield a temperature sensitivity of 12.5, 13.0, 13.7, 14.0, 14.4, 14.8, 15.1, 14.8, 15.1, and 15.2 pm/°C in each temperature range, respectively. Considering the wavelength resolution (0.02 nm) of the employed OSA and a temperature sensitivity of 15 pm/°C, a minimal temperature resolution of the sensor is ~1.3°C. The HCF-tip FPI high-temperature sensor is extremely simple in preparation, and the annealing-free property can reduce the cost significantly, which is promising in mass production and applications.

3. HCF High-Pressure Sensors

In this section, we present two gas pressure sensors based on hollow-core PBG fiber (HC-PBF), which exhibit ultrahigh linearity and sensitivity. Wavelength and phase demodulation methods are compared and applied to these two sensors, respectively.

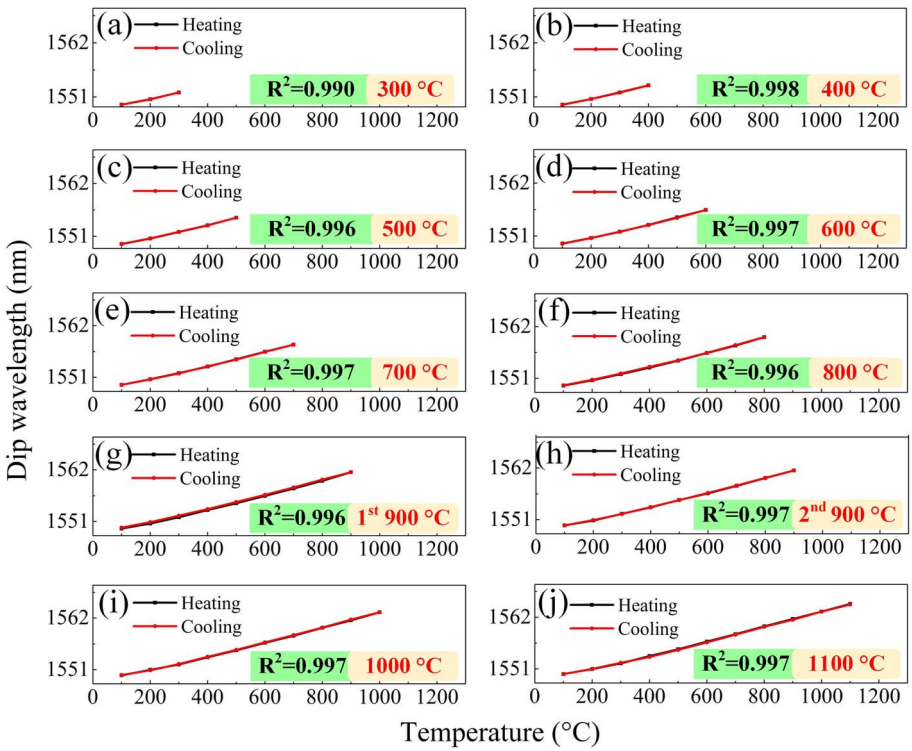

Fig. 9. Wavelength of the tracked dip as a function of temperature for different temperature ranges: (a) 100°C–300°C, (b) 100°C–400°C, (c) 100°C–500°C, (d) 100°C–600°C, (e) 100°C–700°C, (f) 100°C–800°C, (g) first 100°C–900°C, (h) second 100°C–900°C, (i) 100°C–1000°C, and (j) 100°C–1100°C.

3.1. Wavelength-demodulated open-cavity FPI high-pressure sensor

The most common fiber-optic gas pressure sensor is fiber-tip elastic diaphragm FPI, which is an enclosed cavity that is based on a gas pressure-induced deformation of the diaphragm (i.e., cavity length change)[77–83]. However, the diaphragm-type FPI sensors are defective. Firstly, elastic diaphragms have intrinsic elastic limits, beyond which the deformation cannot recover, rendering the pressure sensor a poor resilience and a limited measurement range. Secondly, the evenness of the diaphragm determines the force bearing and deformation of the diaphragm, i.e., the pressure response. As a result, a small unevenness of the diaphragm is fatal for the sensor. Instead, gas-pressure-induced gas RI change is a linear relationship, which provides a better approach to the design and preparation of fiber-optic gas pressure sensors[84–86]. Based on the principle of gas-pressure-induced gas RI change, an open-cavity FPI gas pressure sensor based on HC-PBF is proposed and schematically illustrated in Fig. 10[87]. The sensor is prepared by optimized arc discharge fusion splicing and precision fiber cutting. An HC-PBF is firstly fusion spliced at the end of the lead-in SMF, acting as the cavity of FPI. A length of HCF with an ID of 2 μm is then fusion spliced at the end of the HC-PBF, working as a gas inlet channel to the cavity. Here, the air core of the HC-PBF is ~10.9 μm, and the HCF that is spliced at the HC-PBF end can provide a reflection mirror as well. Tilted slicing is applied to the end of the HCF to eliminate the parasitic reflection. Figure 11 presents the SEM images of the employed HC-PBF and HCF, respectively. It is worth noting that the HCF with a larger ID can speed up the gas intake at the cost of reducing the reflection at the HC-PBF/HCF interface. As a result, the HCF with an ID of 2 μm is a tradeoff. The low-loss property of the HC-PBF makes it possible to construct a long cavity, which renders a sharp peak and a lower detection limit.

Figures 12(a) and 12(b) present the prepared sensors with varying FPI cavity lengths and the corresponding reflection spectra, respectively. A longer cavity with narrower full width at half-wave (FWHW) is available, but not shown for the purpose of brevity. The cavity length and corresponding free spectrum range (FSR) of the six sensor samples are shown in the first two columns of Table 2. The FSR can be denoted as

$$\mathrm{FSR} = \frac{\lambda_1 \lambda_2}{2nL}, \tag{7}$$

where λ_1, λ_2 denote the wavelength of adjacent dips; n and L are the RI of air and the cavity length, respectively. As shown in

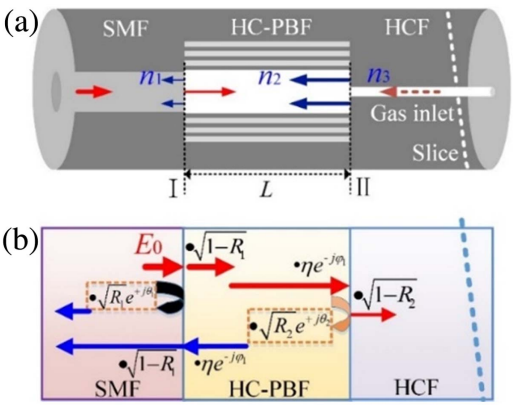

Fig. 10. Schematic diagram of the open-cavity FPI gas pressure sensor based on HC-PBF.

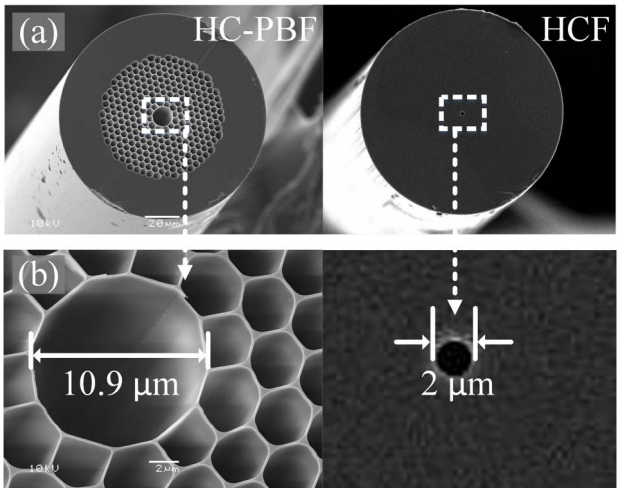

Fig. 11. (a) SEM images of the employed HC-PBF and HCF and (b) locally enlarged view.

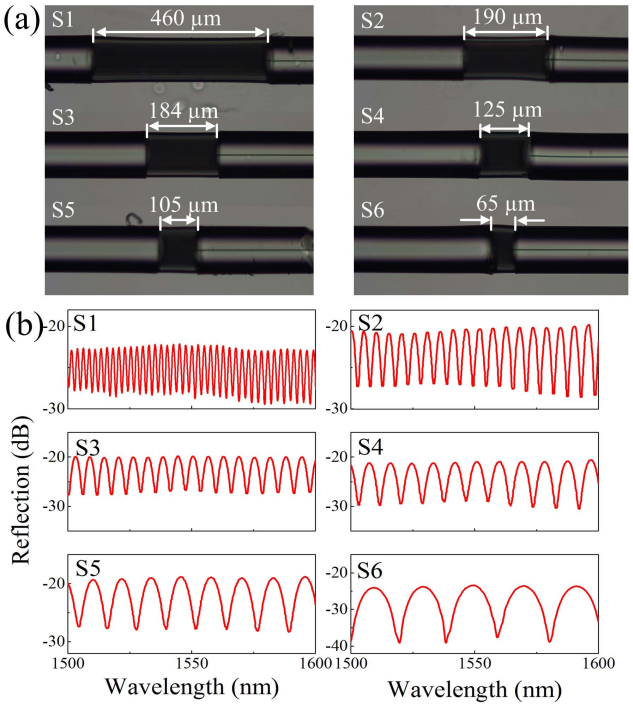

Fig. 12. (a) Microscope images of the prepared sensor samples (S_1–S_6) with varying cavity lengths; (b) the corresponding reflection spectra.

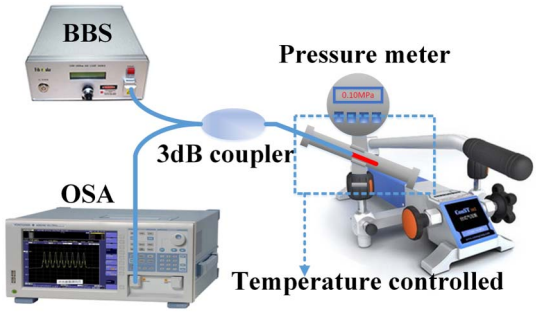

Fig. 13. Schematic illustration of the gas pressure generator.

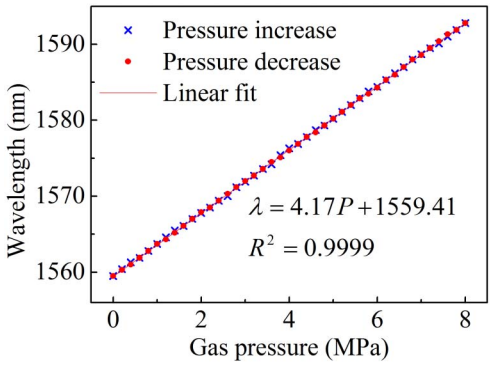

Fig. 14. Wavelength of the tracked dip versus pressure in both the boosting and depressurizing processes.

Fig. 10(b), the reflectivity of the two interfaces I and II can be represented by

$$R_1 = \frac{(n_1 - n_2)^2}{(n_1 + n_2)^2}, \qquad R_2 = \frac{(n_2 - n_3)^2}{(n_2 + n_3)^2}, \tag{8}$$

where n_1, n_2, and n_3 are about 1.46, 1.00, and 1.45, respectively. The reflectivity R_1 and R_2 can then be calculated to be ~0.035 and 0.034, respectively. The low reflectivity ($R \ll 1$) indicates a low-finesse Fabry–Perot cavity. As a result, high-order reflections in the cavity can be negligible, and a two-wave interference approximation is reasonable[88]. As illustrated in Fig. 10(b), E_0 denotes the field intensity of incident light, η is the transmission coefficient of the cavity, φ_1, θ_1, and θ_2 denote the phase change after transmitting through the cavity and the air/silica and silica/air interfaces, respectively. The total reflection intensity can be written as

$$I(\lambda) = I_0\left[R_1 + R_2\eta - 2\sqrt{R_1R_2\eta}\cos\left(\frac{2\pi}{\lambda}nL + \varphi_0\right)\right], \tag{9}$$

where I_0 is the light intensity launched into the Fabry–Perot cavity; n, L, and φ_0 denote the RI of air, the cavity length, and the initial phase difference of the two beams, respectively. The transmission loss of the HC-PBF is low, and $\eta \approx 1$. The reflection spectrum exhibits an approximating sinusoidal curve, which agrees well with the experimental results that are shown in Fig. 12(b).

The sensor samples are encapsulated in the gas cell successively, and the pressure is gradually increased from 0 to 8 MPa in a step of 0.2 MPa. The gas pressure generator is schematically illustrated in Fig. 13. One of the interference dips near 1550 nm is traced as a pressure indicator, and a linear "redshift" is observed as pressure rising. Figure 14 shows the wavelength of the tracked dip versus pressure in both the boosting and depressurizing processes for a sensor with a ~190 μm cavity, where excellent resilience and high sensitivity (~4.17 nm/MPa at ~1560 nm) are definitively confirmed. Moreover, the pressure response of the sensor is rapid with no hysteresis, and the linearity is ultrahigh (0.9999), which is several orders of magnitude higher than that of the diaphragm-based pressure sensor. Further on, less than 0.5 s pressure response time is demonstrated for the sensor by employing a tunable laser, a photoelectric detector (PD), and an oscilloscope. Sensitivities at different wavelengths of the sensor are shown in Fig. 15, where the proportion relationship between wavelength sensitivity and wavelength is confirmed. The performance comparison of six sensor samples is presented in Table 2,

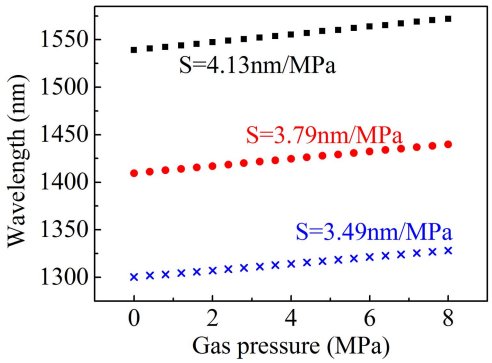

Fig. 15. Gas pressure sensitivities of the sensor at different wavelengths.

Table 2. Performance Comparisons of Sensor Samples with Varying FPI Cavity Lengths.

Cavity Length (μm)	FSR (at ~1550 nm) (nm)	Sensitivity (at ~1550 nm) (nm/MPa)	R^2
65	20.7	4.17	0.9998
105	12.4	4.36	0.9999
125	8.9	4.20	0.9998
184	6.3	4.17	0.9999
190	5.3	4.13	0.9999
460	2.5	4.19	0.9997

which further confirmed the sensor's reliability and high linearity. For discussion, the pressure sensitivity can be written as

$$\frac{\mathrm{d}\lambda}{\mathrm{d}P}=\lambda\left(\frac{1}{L}\frac{\mathrm{d}L}{\mathrm{d}P}+\frac{1}{n}\frac{\mathrm{d}n}{\mathrm{d}P}\right). \tag{10}$$

As pressure increases, the RI of air in the cavity increases according to

$$n=1+\frac{2.8793\times10^{-9}}{1+0.00367\times t}P, \tag{11}$$

where n, P, and t denote the RI of air, the pressure (Pa), and the temperature (°C), respectively. The effect of cavity length change ($\mathrm{d}L/\mathrm{d}P$) is calculated to be less than 0.015 nm/MPa, which can be neglected compared with the sensor's sensitivity of 4.17 nm/MPa.

It is worth noting that the cavity length has nothing to do with the wavelength sensitivity. Meanwhile, a longer cavity renders a much smaller FWHW, which determines the demodulation resolution of the wavelength. Considering a wavelength demodulator with 0.1 pm resolution, an extremely low detection limit of ~23 Pa is available. Moreover, the sensor functioned well at pressures higher than 8 MPa, which is beyond the range of our gas pressure generator.

High-temperature resistance of the high-pressure sensor is studied by high-temperature experiments. The wavelengths of tracked dips are recorded by an optical spectrum analyzer (OSA) over a period of 4 h at a temperature of 800°C. Figure 16 depicts the wavelength of tracked dips versus annealing time at 800°C environments, where excellent thermal resistance is confirmed. Then, the temperature is increased from room temperature (~25°C) to 800°C, and the wavelengths of all the three dips wriggle less than 1 nm, indicating a temperature crosstalk of less than 1 kPa/°C.

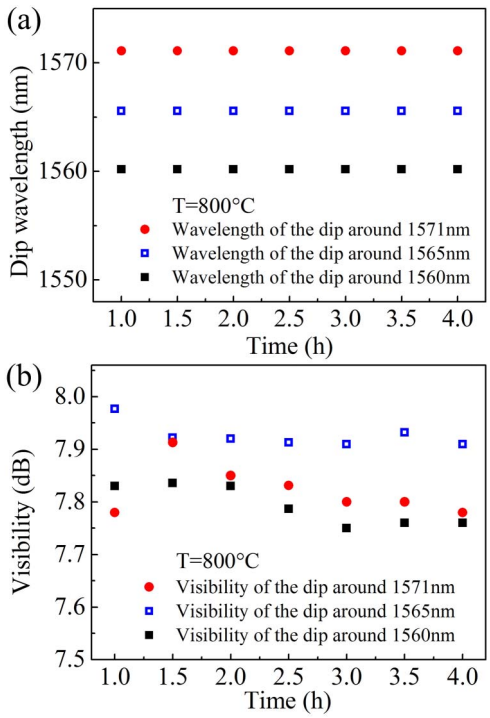

Fig. 16. (a) Wavelength and (b) visibility of the three tracked dips versus annealing time at 800°C.

3.2. Phase-demodulated long-cavity FPI high-pressure sensor

As discussed in Section 3.1, the cavity length of the FPI has nothing to do with the wavelength sensitivity, while the optical phase changing is in proportion to the cavity length. Based on this principle, we propose an ultralong air-cavity fiber FPI sensor based on HC-PBF and phase demodulation method in this section. The sensor structure is similar to Fig. 10, where the only difference is a longer cavity (i.e., longer HC-PBF) and the phase demodulation approach. The low-loss HC-PBFs enable a long air cavity without large compromise for the fringe visibility. Four sensor samples (S_1, S_2, S_3, and S_4) with cavity lengths of 107 μm, 1.1 mm, 2.1 mm, and 12.3 mm are prepared, respectively, the reflection spectra of which are measured and shown in Fig. 17. In order to confirm the vital function of the HC-PBF for a long-cavity FPI, the reflection spectrum (S_4) within and beyond the PBG of the HC-PBF is compared and shown in Fig. 18, where we can clearly see that a low-loss cavity is vital for a long-cavity FPI.

Theory calculation of the phase sensitivity of the sensor is performed, and phase difference of the two beams can be represented by the OPD between the two beams, which can be expressed by

$$\mathrm{OPD}=2n(P,T)L. \tag{12}$$

Here, L and $n(P,T)$ denote the cavity length and the RI of gas, respectively. For standard air, the RI can be expressed as a simple function of the pressure P (Pa) and temperature T (°C), as shown in Eq. (11). For constant temperature and gas species, the n as well as OPD increases linearly with pressure P. In other words, if we extract the information of OPD from the spectra,

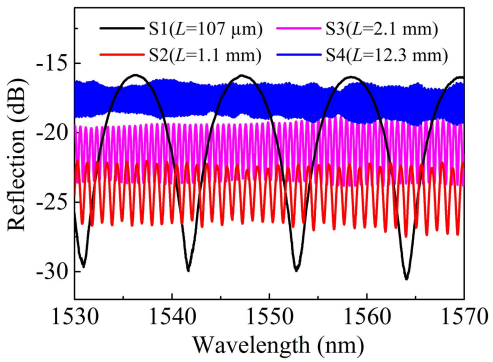

Fig. 17. Reflection spectra of the prepared sensor samples with different cavity lengths (S_1: 107 μm, S_2: 1.1 mm, S_3: 2.1 mm, and S_4: 12.3 mm).

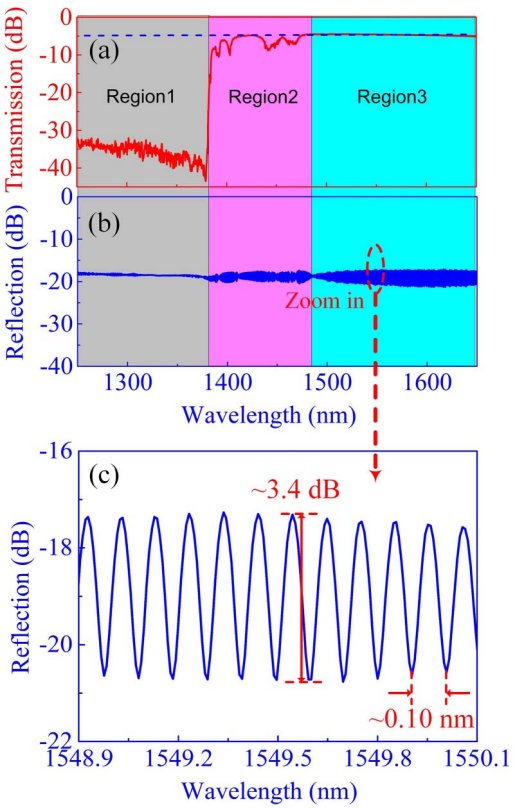

Fig. 18. Measured (a) transmission and (b) reflection spectra of the FPI with a 12.3 mm cavity; (c) enlarged view of the FPI reflection spectrum at ~1550 nm.

the gas pressure can be interrogated. The pressure sensitivity S can be expressed as

$$S=\frac{\delta(\mathrm{OPD})}{\delta(P)}=\frac{\delta(\mathrm{OPD})}{\delta(n)}\frac{\delta(n)}{\delta(P)}=2L\frac{2.8793\times10^{-9}}{1+0.00367t}. \tag{13}$$

The OPD versus gas RI for different cavity lengths L can be calculated and is plotted in Fig. 19, where a linear relationship between the phase sensitivity and cavity length can be confirmed.

The same setup as above is employed for gas pressure tests. Four prepared sensor samples S_1–S_4 are subsequently sealed into an air chamber, respectively, where the temperature is kept at 25°C for the whole time. The gas pressure is increased from standard atmospheric pressure to 4 MPa in a step of 0.5 MPa. At each measured point, the reflection spectra are recorded by the OSA. The Fourier phase interrogation method reported in Refs. [37,89,90] is applied to the recorded reflection spectra, and the OPD change with respect to the gas pressure is illustrated in Figs. 20(a)–20(d), where the gas pressure sensitivities (by linear fitting) are 0.55, 6.01, 10.14, and 61.70 μm/MPa, respectively. With the elongating of the cavity, the sensitivity exhibits a linear increase, where the linearity is higher than 0.99, confirming the accuracy of the employed phase interrogation method.

The sensor performance at a higher gas pressure of 0.1–10 MPa is further studied. Another four sensor samples (S_5, S_6, S_7, and S_8) with cavity lengths of 2.7, 6.7, 12.4, and 24.9 mm, respectively, are prepared and tested. The OPD versus gas pressure is shown in Fig. 21, where linear fits yield a high linearity of 0.999, 0.998, 0.999, and 0.999, respectively. A linear relationship between the sensitivity and cavity length is convincing as well. Figure 22 exhibits the measured gas pressure sensitivities of all eight sensor samples (S_1–S_8) as a function of the cavity lengths L, and the results agree well with the theoretical predictions. It is worth noting that the proposed sensor can withstand a higher pressure, which has not been explored due to the equipment limitation. Anyway, the combination of the long air cavity FPI and phase interrogation method renders a high-quality high-pressure sensor. For other gas species, the gas pressure can be simply interrogated by a modified relationship from Eq. (11).

4. Simultaneous Measurement of High Temperature and High Pressure Using an HCF Dual-Cavity FPI

As demonstrated in the last two sections, silica and air cavities present excellent high-temperature and high-pressure responses, respectively. As such, a silica/air hybrid cavity may address the issue of simultaneous measurement of high temperature and high pressure. Figure 23(a) shows a schematic of a silica/air dual-cavity FPI sensor configuration, where the HC-PBF acts as the air cavity (cavity 1), while the HCF acts as both

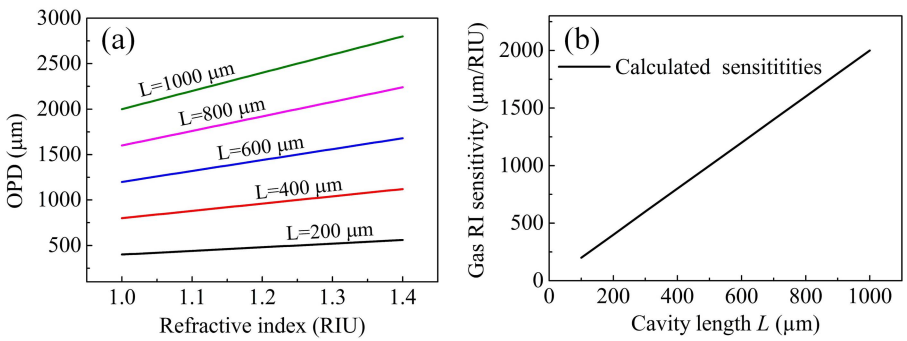

Fig. 19. (a) Calculated OPDs of FPIs with different cavity lengths L as a function of the gas RI; (b) calculated gas RI sensitivity versus FPI cavity length L.

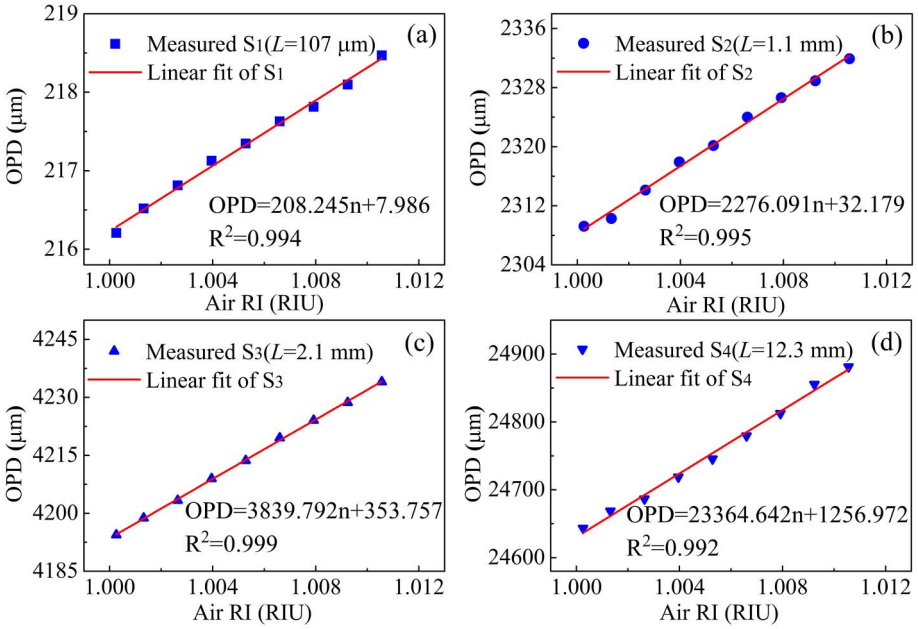

Fig. 20. Demodulated OPDs of the four sensor samples as a function of the gas pressure in a range of 0.1–4.0 MPa: (a) S_1 (L = 107 μm), (b) S_2 (L = 1.1 mm), (c) S_3 (L = 2.1 mm), and (d) S_4 (L = 12.3 mm).

the silica cavity (cavity 2) and vessel for the gas inlet simultaneously. The sensor structure has no significant change in comparison with the sensor described in the last chapter, except for the addition of reflection interface III. As such, the vital task locates in the separation and interrogation of the superimposed interference spectrum.

Four sensor samples (S_1–S_4) with different cavity length combinations are prepared, and the morphologies as well as the corresponding reflection spectra are illustrated in Fig. 24. The cavity length combinations of S_1–S_4 are 226/634, 261/751, 242/957, and 621/1491 μm, respectively, and the reflection spectra are all characterized by fine fringes modulated by large envelopes, indicating multibeam interference. As demonstrated in the last chapter, the OPDs of the silica and air cavity are sensitive to the temperature and gas pressure, respectively. The crosstalk of temperature and pressure can be estimated to be 268 Pa/°C at the atmospheric pressure and 100°C by Eq. (11). As a result, cavity 1 can be utilized as a gas pressure sensor. In contrast, the

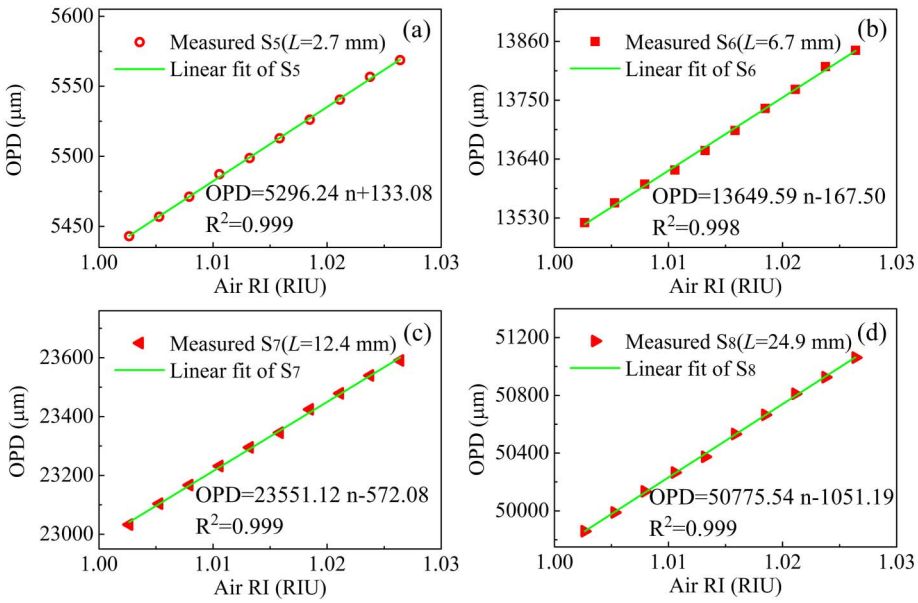

Fig. 21. Demodulated OPDs of four sensor samples as a function of the gas pressure in a range of 1–10 MPa: (a) S_5 (L = 2.7 mm), (b) S_6 (L = 6.7 mm), (c) S_7 (L = 12.4 mm), and (d) S_8 (L = 24.9 mm).

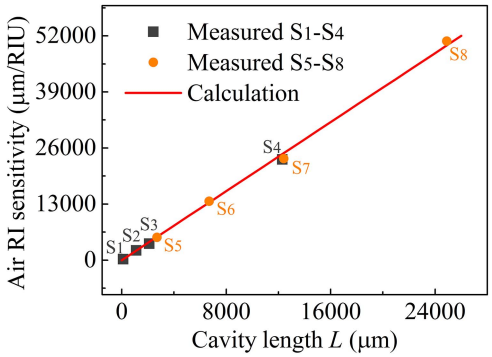

Fig. 22. Gas pressure sensitivities of the eight sensor samples (S_1–S_8) as a function of the cavity length L.

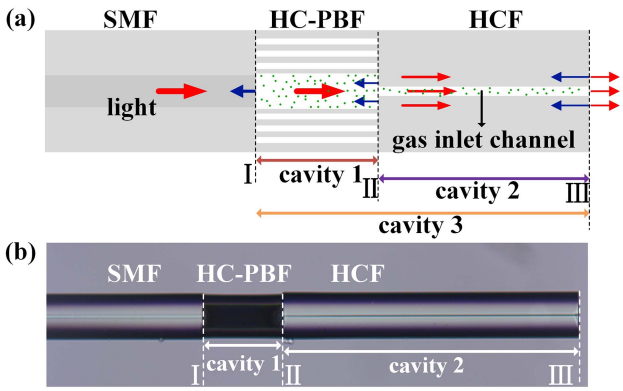

Fig. 23. (a) Schematic diagram of the proposed dual-cavity FPI sensor; (b) sideview microscopy of the sensor.

OPD of cavity 2 changes significantly with temperature, while it hardly changes with the gas pressure. As such, cavity 2 can be employed as a temperature indicator. For interrogating the OPDs of the two cavities respectively, an FFT and frequency filtering method is applied to the superimposed interference spectrum.

The reflection spectrum of S_1 at room temperature and atmospheric pressure is presented in Fig. 25(a). Figure 25(b) shows the FFT results of the spectrum that are shown in Fig. 25(a), which is characterized by three frequency components of ~0.2, 0.8, and 1.0. As a result, two bandpass filters (0.1–0.3 Hz and 0.7–0.9 Hz) are subsequently applied to the superimposed reflection spectra, and the individual spectra of cavity 1 and cavity 2 are separated and displayed in Figs. 25(c) and 25(d), respectively. The phase shift $\Delta\varphi$ results from wavelength scanning from λ_1 to λ_2 can be obtained by the Fourier phase interrogation method[89,90]. When λ_1, λ_2, and $\Delta\varphi$ are determined, the absolute OPD can be obtained according to

$$\mathrm{OPD} = \frac{\lambda_1\lambda_2}{4\pi(\lambda_1 - \lambda_2)}\Delta\varphi. \tag{14}$$

Sensor sample S_1 is chosen for the high-temperature and high-pressure tests. The gas pressure is firstly increased from 0 to 10 MPa with a step size of 1 MPa. At each step, the reflection spectrum is recorded, and the OPDs of the two cavities are interrogated, respectively, by the approach described above. Figure 26 exhibits the pressure sensitivities of the two cavities, where the pressure sensitivity of cavity 1 (~1.336 μm/MPa) is nearly two orders of magnitude higher than that of cavity 2 (~0.008 μm/MPa). Temperature measurement in both the heating and cooling processes within 100°C–800°C is subsequently

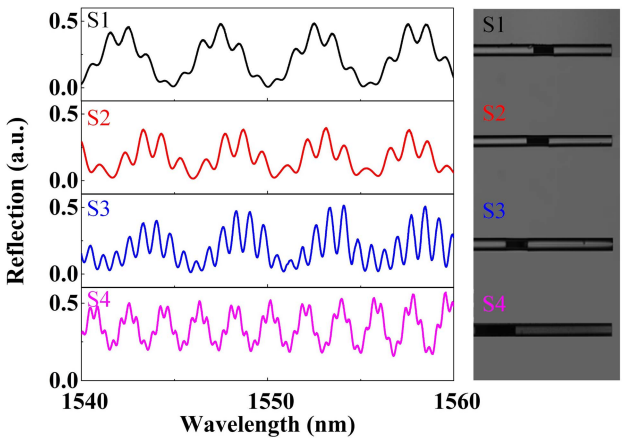

Fig. 24. Reflection spectra and the corresponding microscopy images of the four fabricated dual-cavity FPI sensors (S_1–S_4) with different combinations of cavity lengths.

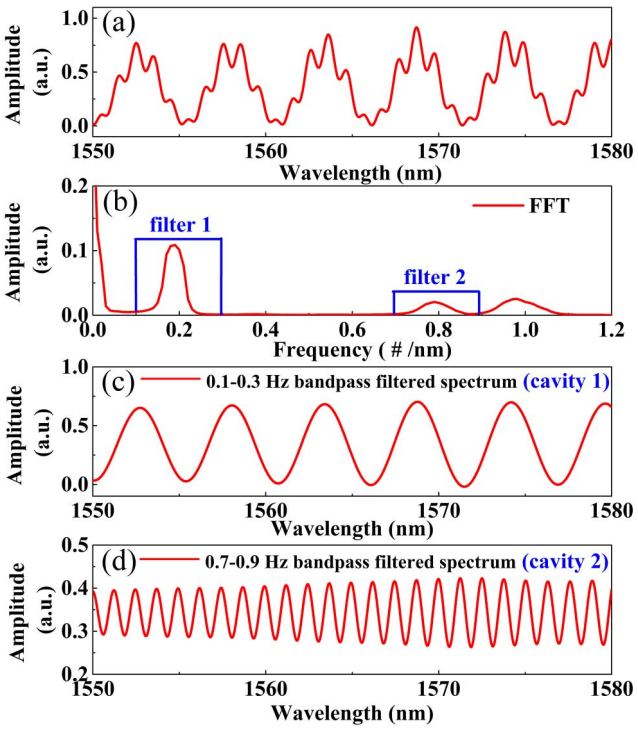

Fig. 25. (a) Reflection spectrum of S_1 and (b) the FFT spectrum of (a); also shown are the separated reflection spectra of (c) cavity 1 and (d) cavity 2, respectively, by bandpass filtering.

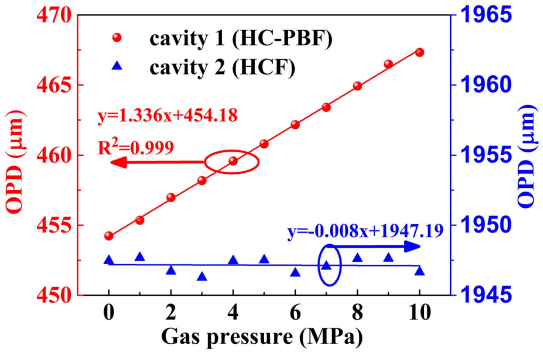

Fig. 26. OPD of the two cavities as a function of gas pressure.

carried out, and repeated temperature cycles are performed. The relationship between the interrogated OPD and temperature is obtained by a linear fitting and plotted in Fig. 27, where the temperature sensitivity of cavity 2 (~17 nm/°C) is approximately two orders of magnitude higher than that of cavity 1 (~0.1 nm/°C).

According to the experimental results, the temperature drift is calculated to be ~74 Pa/°C for cavity 1, which is about two orders of magnitude smaller than the errors in our previous work[83]. Meanwhile, the temperature measurement error results from the pressure change of ~0.47°C/MPa, which is small enough to be neglected. However, the linearity for temperature measurement is poor, which can be attributed to an environment-induced phase shift during the spectrum acquisition. Further improvement is ongoing, which is focused on decreasing the environment-induced phase shift during the collection of spectra. Sensor S_1 is taken out after the high-temperature and high-pressure tests, and the microscope morphology of S_1 is shown in Fig. 28, where the sensor shows no damage, confirming the robustness and reusability of the sensor.

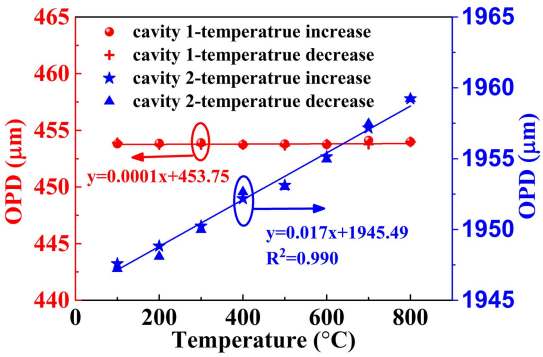

Fig. 27. OPD of the two cavities as a function of temperature.

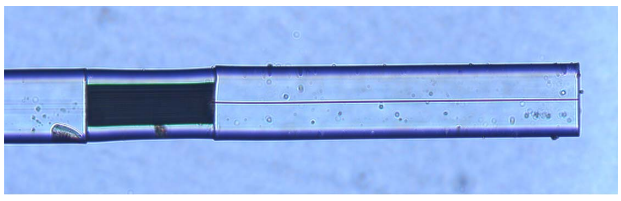

Fig. 28. Microscopy image of the sensor S_1 after conducting high-pressure and high-temperature tests.

5. Conclusion

In summary, this paper reviewed our recent works on high-temperature and high-pressure sensing technologies based on HCFs. A variety of sensor structures, different sensing mechanisms, and demodulation methods are detailed. Further improvements may be located in the fast and dynamic demodulation techniques of temperature and pressure, which can eliminate the environment-induced phase shift effectively and meet the critical demand for dynamic measurement of high temperature and high pressure. In addition, the package techniques of the fiber-optic high-temperature and high-pressure sensors are equally important for practical applications. It is worth noting that the high-temperature and high-pressure sensing techniques reviewed in this paper are merely a small part of the many applications of HCFs. The technical advancements of HCFs achieved in recent years have accelerated the growth of HCFs and their applications significantly. More and more vital applications of HCFs in extreme environment sensing can be expected in the coming decade.

Acknowledgement

This work was supported by the National Natural Science Foundation of China (NSFC) (Nos. 61875128 and 61635007), China Postdoctoral Science Foundation (No. 2020M683184), Guangdong Basic and Applied Basic Research Foundation (No. 2021B1515020030), Department of Science and Technology of Guangdong Province (No. 2019TQ05X113), and Shenzhen Science and Technology Program (No. RCYX20200714114538160).

References

1. G. B. Hocker, "Fiber-optic sensing of pressure and temperature," Appl. Opt. **18**, 1445 (1979).
2. A. K. Sharma, R. Jha, and B. D. Gupta, "Fiber-optic sensors based on surface plasmon resonance: a comprehensive review," IEEE Sens. J. **7**, 1118 (2007).
3. A. Leung, P. M. Shankar, and R. Mutharasan, "A review of fiber-optic biosensors," Sens. Actuat. B: Chem. **125**, 688 (2007).
4. M. Majumder, T. K. Gangopadhyay, A. K. Chakraborty, K. Dasgupta, and D. K. Bhattacharya, "Fiber Bragg gratings in structural health monitoring —present status and applications," Sens. Actuat. A: Phys. **147**, 150 (2008).
5. S. J. Mihailov, "Fiber Bragg grating sensors for harsh environments," Sensors **12**, 1898 (2012).
6. J. Albert, L. Y. Shao, and C. Caucheteur, "Tilted fiber Bragg grating sensors," Laser Photon. Rev. **7**, 83 (2013).
7. X. J. Fan, J. F. Jiang, X. Z. Zhang, K. Liu, and T. G. Liu, "Investigation on temperature characteristics of weak fiber Bragg gratings in a wide range," Chin. Opt. Lett. **17**, 120603 (2019).
8. Y. M. Zhang, D. D. Rong, L. Q. Zhu, M. L. Dong, and F. Luo, "Regenerated fiber Bragg grating for fiber laser sensing at high temperatures," Chin. Opt. Lett. **16**, 040606 (2018).

9. C. W. Smelser, S. J. Mihailov, and D. Grobnic, "Formation of type I-IR and Type II-IR gratings with an ultrafast IR laser and a phase mask," Opt. Express **13**, 5377 (2005).
10. Y. Wang, Y. H. Li, C. R. Liao, D. N. Wang, M. W. Yang, and P. X. Lu, "High-temperature sensing using miniaturized fiber in-line Mach–Zehnder interferometer," IEEE Photon. Technol. Lett. **22**, 39 (2009).
11. S. C. Warren-Smith, L. V. Nguyen, C. Lang, H. E. Heidepriem, and T. M. Monro, "Temperature sensing up to 1300°C using suspended-core microstructured optical fibers," Opt. Express **24**, 3714 (2016).
12. C. Wang, J. C. Zhang, C. Z. Zhang, J. He, Y. C. Lin, W. Jin, C. R. Liao, Y. Wang, and Y. P. Wang, "Bragg gratings in suspended-core photonic microcells for high-temperature applications," J. Lightwave Technol. **36**, 2920 (2018).
13. J. He, Y. P. Wang, C. R. Liao, C. Wang, S. Liu, K. M. Yang, Y. Wang, X. C. Yuan, G. P. Wang, and W. J. Zhang, "Negative-index gratings formed by femtosecond laser overexposure and thermal regeneration," Sci. Rep. **6**, 23379 (2016).
14. S. Liu, L. Jin, W. Jin, D. N. Wang, C. R. Liao, and Y. Wang, "Structural long period gratings made by drilling micro-holes in photonic crystal fibers with a femtosecond infrared laser," Opt. Express **18**, 5496 (2010).
15. D. Grobnic, S. J. Mihailov, C. W. Smelser, and H. Ding, "Sapphire fiber Bragg grating sensor made using femtosecond laser radiation for ultrahigh temperature applications," IEEE Photon. Technol. Lett. **16**, 2505 (2004).
16. M. Busch, W. Ecke, I. Latka, D. Fischer, R. Willsch, and H. Bartelt, "Inscription and characterization of Bragg gratings in single-crystal sapphire optical fibers for high-temperature sensor applications," Meas. Sci. Technol. **20**, 115301 (2009).
17. T. Elsmann, T. Habisreuther, A. Graf, M. Rothhardt, and H. Bartelt, "Inscription of first-order sapphire Bragg gratings using 400 nm femtosecond laser radiation," Opt. Express **21**, 4591 (2013).
18. T. Habisreuther, T. Elsmann, Z. Pan, Z. Graf, R. Willsch, and M. A. Schmidt, "Sapphire fiber Bragg gratings for high temperature and dynamic temperature diagnostics," Appl. Therm. Eng. **91**, 860 (2015).
19. S. Yang, D. Hu, and A. B. Wang, "Point-by-point fabrication and characterization of sapphire fiber Bragg gratings," Opt. Lett. **42**, 4219 (2017).
20. C. Chen, X. Y. Zhang, Y. S. Yu, W. H. Wei, Q. Guo, L. Qin, Y. Q. Ning, L. J. Wang, and H. B. Sun, "Femtosecond laser-inscribed high-order Bragg gratings in large-diameter sapphire fibers for high-temperature and strain sensing," J. Lightwave Technol. **36**, 3302 (2018).
21. X. Z. Xu, J. He, C. R. Liao, K. M. Yang, K. K. Guo, C. Li, Y. F. Zhang, Z. B. Ouyang, and Y. P. Wang, "Sapphire fiber Bragg gratings inscribed with a femtosecond laser line-by-line scanning technique," Opt. Lett. **43**, 4562 (2018).
22. X. W. Shu, Z. Lin, and I. Bennion, "Sensitivity characteristics of long-period fiber gratings," J. Lightwave Technol. **20**, 255 (2002).
23. Y. J. Rao, Z. L. Ran, X. Liao, and H. Y. Deng, "Hybrid LPFG/MEFPI sensor for simultaneous measurement of high-temperature and strain," Opt. Express **15**, 14936 (2007).
24. Y. J. Rao, Y. P. Wang, Z. L. Ran, and T. Zhu, "Novel fiber-optic sensors based on long-period fiber gratings written by high-frequency CO_2 laser pulses," J. Lightwave Technol. **21**, 1320 (2003).
25. G. Rego, O. Okhotnikov, E. Dianov, and V. Sulimov, "High-temperature stability of long-period fiber gratings produced using an electric arc," J. Lightwave Technol. **19**, 1574 (2001).
26. G. Rego, "Arc-induced long-period fiber gratings," J. Sens. **2016**, 3598634 (2016).
27. G. Humbert and A. Malki, "Characterizations at very high temperature of electric arc-induced long-period fiber gratings," Opt. Commun. **208**, 329 (2002).
28. L. Jiang, J. Yang, S. Wang, B. Li, and M. Wang, "Fiber Mach–Zehnder interferometer based on microcavities for high-temperature sensing with high sensitivity," Opt. Lett. **36**, 3753 (2011).
29. N. Zhao, Q. J. Lin, W. X. Jing, Z. D. Jiang, Z. R. Wu, K. Yao, B. Tian, Z. K. Zhang, and P. Shi, "High temperature high sensitivity Mach–Zehnder interferometer based on waist-enlarged fiber bitapers," Sens. Actuat. A: Phys. **267**, 491 (2017).
30. A. A. Jasim, S. W. Harun, H. Arof, and H. Ahmad, "Inline microfiber Mach–Zehnder interferometer for high temperature sensing," IEEE Sens. J. **13**, 626 (2013).
31. Z. Zhang, C. R. Liao, J. Tang, Y. Wang, Z. Y. Bai, Z. Y. Li, K. K. Guo, M. Deng, S. Q. Cao, and Y. P. Wang, "Hollow-core-fiber-based interferometer for high temperature measurement," IEEE Photon. J. **9**, 7101109 (2017).
32. J. Zhang, H. Sun, Q. Z. Rong, and X. G. Qiao, "High-temperature sensor using a Fabry–Perot interferometer based on solid-core photonic crystal fiber," Chin. Opt. Lett. **10**, 070607 (2012).
33. P. Chen and X. W. Shu, "Refractive-index-modified-dot Fabry–Perot fiber probe fabricated by femtosecond laser for high-temperature sensing," Opt. Express **26**, 5292 (2018).
34. D. W. Duan, Y. J. Rao, W. Wen, J. Yao, D. Wu, L. Xu, and T. Zhu, "In-line all-fiber Fabry–Perot interferometer high temperature sensor formed by large lateral offset splicing," Electronics **47**, 401 (2011).
35. Z. S. Chen, S. S. Xiong, S. C. Gao, H. Zhang, L. Wan, X. C. Huang, B. S. Huang, Y. H. Feng, W. P. Liu, and Z. H. Li, "High-temperature sensor based on Fabry–Perot interferometer in microfiber tip," Sensors **18**, C1 (2018).
36. X. L. Tan, Y. F. Geng, X. J. Li, G. Rong, and Z. Yin, "High temperature microstructured fiber sensor based on a partial-reflection-enabled intrinsic Fabry–Perot interferometer," Appl. Opt. **52**, 8195 (2013).
37. Z. Zhang, J. He, B. Du, F. C. Zhang, K. K. Guo, and Y. P. Wang, "Measurement of high pressure and high temperature using a dual-cavity Fabry–Perot interferometer created in cascade hollow-core fibers," Opt. Lett. **43**, 6009 (2018).
38. Z. Zhang, B. J. Xu, M. Zhou, W. J. Bao, X. Z. Xu, and Y. P. Wang, "Hollow-core fiber-tip interferometric high-temperature sensor operating at 1100°C," Micromachines **12**, 234 (2021).
39. Y. H. Li, C. R. Liao, D. N. Wang, T. Sun, and K. Grattan, "Study of spectral and annealing properties of fiber Bragg gratings written in H_2-free and H_2-loaded fibers by use of femtosecond laser pulses," Opt. Express **16**, 21239 (2008).
40. D. Grobnic, C. Smelser, S. Mihailov, and R. Walker, "Long-term thermal stability tests at 1000°C of silica fiber Bragg gratings made with ultrafast laser radiation," Meas. Sci. Technol. **17**, 1009 (2006).
41. U. Paek and C. Kurkjian, "Calculation of cooling rate and induced stresses in drawing of optical fibers," J. Am. Ceram. Soc. **58**, 330 (1975).
42. D. Wissuchek, C. Ponader, and J. Price, "Analysis of residual stress in optical fiber," Proc. SPIE **3848**, 34 (1999).
43. Y. H. Li, M. W. Yang, D. N. Wang, J. Lu, T. Sun, and K. Grattan, "Fiber Bragg gratings with enhanced thermal stability by residual stress relaxation," Opt. Express **17**, 19785 (2008).
44. R. F. Cregan, B. Mangan, J. C. Knight, T. A. Birks, P. St.J. Russell, P. J. Roberts, and D. C. Allan, "Single-mode photonic bandgap guidance of light in air," Science **285**, 1537 (1999).
45. P. J. Roberts, F. Couny, H. Sabert, B. J. Mangan, D. P. Williams, L. Farr, M. W. Mason, A. Tomlinson, T. A. Birks, J. C. Knight, and P. St.J. Russell, "Ultimate low loss of hollow-core photonic crystal fibers," Opt. Express **13**, 236 (2005).
46. Y. Y. Wang, N. V. Wheeler, F. Couny, P. J. Roberts, and F. Benabid, "Low loss broadband transmission in hypocycloid-core kagome hollow-core photonic crystal fiber," Opt. Lett. **36**, 669 (2011).
47. Poletti and Francesco, "Nested antiresonant nodeless hollow core fiber," Opt. Express **22**, 23807 (2014).
48. Y. Fei and J. C. Knight, "Negative curvature hollow core optical fiber," IEEE J. Sel. Top. Quantum Electron. **22**, 4400610 (2015).
49. S. F. Gao, Y. Y. Wang, W. Ding, D. L. Jiang, S. Gu, and X. Zhang, "Hollow-core conjoined-tube negative-curvature fiber with ultralow loss," Nat. Commun. **9**, 2828 (2018).
50. Y. Y. Wang, X. Peng, M. Alharbi, C. Fourcade Dutin, T. D. Bradley, F. Gérôme, Mielke Michael, Booth Timothy, and F. Benabid, "Design and fabrication of hollow-core photonic crystal fibers for high-power ultrashort pulse transportation and pulse compression," Opt. Lett. **37**, 3111 (2012).
51. C. M. Smith, N. Venkataraman, M. T. Gallagher, D. Müller, J. A. West, N. F. Borrelli, D. C. Allan, and K. W. Koch, "Low-loss hollow-core silica/air photonic bandgap fiber," Nature **424**, 657 (2003).
52. F. Couny, F. Benabid, and P. S. Light, "Large-pitch Kagome-structured hollow-core photonic crystal fiber," Opt. Lett. **31**, 3574 (2006).
53. C. He, C. Zhou, Q. Zhou, S. Y. Xie, and Y. Yao, "Simultaneous measurement of strain and temperature using Fabry–Pérot interferometry and antiresonant mechanism in a hollow-core fiber," Chin. Opt. Lett. **19**, 041201 (2021).

54. F. Benabid, F. Couny, J. Knight, T. Birks, and P. Russell, "Compact, stable and efficient all-fiber gas cells using hollow-core photonic crystal fibers," Nature **434**, 488 (2005).
55. R. Thapa, K. Knabe, K. L. Corwin, and B. R. Washburn, "Arc fusion splicing of hollow-core photonic bandgap fibers for gas-filled fiber cells," Opt. Express **14**, 9576 (2006).
56. C. J. Hensley, D. H. Broaddus, C. B. Schaf, and A. L. Gaeta, "Photonic band-gap fiber gas cell fabricated using femtosecond micromachining," Opt. Express **15**, 6690 (2007).
57. G. Epple, K. S. Kleinbach, T. G. Euser, N. Y. Joly, T. Pfau, P. Russell, and R. Low, "Rydberg atoms in hollow-core photonic crystal fibers," Nat. Commun. **5**, 4132 (2014).
58. K. K. Chow, M. Short, S. Lam, A. Mcwilliams, and H. Zeng, "A Raman cell based on hollow core photonic crystal fiber for human breath analysis," Med. Phys. **41**, 092701 (2014).
59. P. S. Light, F. Couny, and F. Benabid, "Low optical insertion-loss and vacuum-pressure all-fiber acetylene cell based on hollow-core photonic crystal fiber," Opt. Lett. **31**, 2538 (2006).
60. M. P. Buric, K. P. Chen, J. Falk, and S. D. Woodruff, "Enhanced spontaneous Raman scattering and gas composition analysis using a photonic crystal fiber," Appl. Opt. **47**, 4255 (2008).
61. L. W. Kornaszewski, N. Gayraud, J. M. Stone, W. N. Macpherson, A. K. George, and J. C. Knight, "Mid-infrared methane detection in a photonic bandgap fiber using a broadband optical parametric oscillator," Opt. Express **15**, 11219 (2007).
62. J. P. Parry, B. C. Griffiths, N. Gayraud, E. D. Mcnaghten, A. M. Parkes, and W. N. Macpherson, "Towards practical gas sensing with micro-structured fibers," Meas. Sci. Technol. **20**, 075301 (2009).
63. I. Shavrin, S. Novotny, A. Shevchenko, and H. Ludvigsen, "Gas refractometry using a hollow-core photonic bandgap fiber in a Mach–Zehnder-type interferometer," Appl. Phys. Lett. **100**, 051106 (2012).
64. P. C. Zhao, H. L. Ho, W. Jin, S. C. Fan, S. F. Gao, Y. Y. Wang, and P. Wang, "Gas sensing with mode-phase-difference photothermal spectroscopy assisted by a long period grating in a dual-mode negative-curvature hollow-core optical fiber," Opt. Lett. **45**, 5660 (2020).
65. F. F. Chen, S. L. Jiang, W. Jin, H. H. Bao, H. L. Ho, C. Wang, and S. F. Gao, "Ethane detection with mid-infrared hollow-core fiber photothermal spectroscopy," Opt. Express **28**, 38115 (2020).
66. W. Jin, H. F. Xuan, and H. L. Ho, "Sensing with hollow-core photonic bandgap fibers," Meas. Sci. Technol. **21**, 094014 (2010).
67. Y. Y. Huang, Y. Xu, and A. Yariv, "Fabrication of functional microstructured optical fibers through a selective-filling technique," Appl. Phys. Lett. **85**, 5182 (2004).
68. Z. B. Liu, X. He, and D. N. Wang, "Passively mode-locked fiber laser based on a hollow-core photonic crystal fiber filled with few-layered graphene oxide solution," Opt. Lett. **36**, 3024 (2011).
69. C. Cordeiro, E. Santos, C. Cruz, C. Matos, and D. S. Ferreiira, "Lateral access to the holes of photonic crystal fibers—selective filling and sensing applications," Opt. Express **14**, 8403 (2006).
70. S. T. Bauerschmidt, D. Novoa, B. M. Trabold, A. Abdolvand, and P. Russell, "Supercontinuum up-conversion via molecular modulation in gas-filled hollow-core PCF," Opt. Express **22**, 20566 (2014).
71. A. Hoffmann, M. Zürch, and C. Spielmann, "Extremely nonlinear optics using shaped pulses spectrally broadened in an argon- or sulfur hexafluoride-filled, hollow-core fiber," Appl. Sci. **5**, 1310 (2015).
72. D. Yan, J. Popp, M. W. Pletz, and T. Frosch, "Highly sensitive broadband Raman sensing of antibiotics in step-index hollow-core photonic crystal fibers," ACS Photon. **4**, 138 (2017).
73. M. Gebhardt, T. Heuermann, R. Klas, C. Liu, and J. Limpert, "Bright, high-repetition-rate water window soft x-ray source enabled by nonlinear pulse self-compression in an antiresonant hollow-core fiber," Light: Sci. Appl. **10**, 36 (2021).
74. J. H. Wray and J. T. Neu, "Refractive index of several glasses as a function of wavelength and temperature," J. Opt. Soc. Am. **59**, 774 (1969).
75. B. Kuhn and R. Schadrack, "Thermal expansion of synthetic fused silica as a function of OH content and fictive temperature," J. Non-Crystall. Solids **355**, 323 (2009).
76. M. Ferreira, L. Coelho, K. Schuster, J. Kobelke, L. Santos, and O. Frazão, "Fabry–Perot cavity based on a diaphragm-free hollow-core silica tube," Opt. Lett. **36**, 4029 (2011).
77. H. Bae and M. Yu, "Miniature Fabry–Perot pressure sensor created by using UV-molding process with an optical fiber-based mold," Opt. Express **20**, 14573 (2012).
78. W. H. Wang, N. Wu, Y. Tian, C. Niezrecki, and X. W. Wang, "Miniature all-silica optical fiber pressure sensor with an ultrathin uniform diaphragm," Opt. Express **18**, 9006 (2010).
79. F. Xu, D. X. Ren, X. L. Shi, C. Li, W. W. Lu, L. Lu, L. Lu, and B. L. Yu, "High-sensitivity Fabry–Perot interferometric pressure sensor based on a nanothick silver diaphragm," Opt. Lett. **37**, 133 (2012).
80. J. Ma, J. Ju, L. Jin, and W. Jin, "A compact fiber-tip micro-cavity sensor for high-pressure measurement," IEEE Photon. Technol. Lett. **23**, 1561 (2011).
81. J. Ma, W. Jin, H. L. Ho, and J. Y. Dai, "High-sensitivity fiber-tip pressure sensor with graphene diaphragm," Opt. Lett. **37**, 2493 (2012).
82. J. C. Xu, X. W. Wang, K. L. Cooper, and A. B. Wang, "Miniature all-silica fiber optic pressure and acoustic sensors," Opt. Lett. **30**, 3269 (2005).
83. Z. Zhang, C. R. Liao, J. Tang, Z. Y. Bai, K. K. Guo, M. X. Hou, J. He, Y. Wang, S. Liu, F. Zhang, and Y. P. Wang, "High-sensitivity gas-pressure sensor based on fiber-tip PVC diaphragm Fabry–Perot interferometer," J. Lightwave Technol. **35**, 4067 (2017).
84. M. Deng, C. P. Tang, T. Zhu, Y. J. Rao, L. C. Xu, and M. Han, "Refractive index measurement using photonic crystal fiber-based Fabry–Perot interferometer," Appl. Opt. **49**, 1593 (2010).
85. J. Tang, G. L. Yin, C. R. Liao, S. Liu, Z. Y. Li, X. Y. Zhong, Q. Wang, J. Zhao, K. M. Yang, and Y. P. Wang, "High-sensitivity gas pressure sensor based on Fabry–Perot interferometer with a side-opened channel in hollow-core photonic bandgap fiber," IEEE Photon. J. **7**, 2489926 (2015).
86. Y. C. Cao, W. Jin, F. Yang, and H. L. Ho, "Phase sensitivity of fundamental mode of hollow core photonic bandgap fiber to internal gas pressure," Opt. Express **22**, 13190 (2014).
87. Z. Zhang, J. He, Q. Dong, Z. Y. Bai, C. R. Liao, Y. Wang, S. Liu, K. K. Guo, and Y. P. Wang, "Diaphragm-free gas-pressure sensor probe based on a hollow-core photonic bandgap fiber," Opt. Lett. **43**, 3017 (2018).
88. J. Ma, *Miniature Fiber-Tip Fabry–Perot Interferometric Sensors for Pressure and Acoustic Detection* (The Hong Kong Polytechnic University, 2014).
89. Y. Jiang, "Fourier transform white-light interferometry for the measurement of fiber-optic extrinsic Fabry–Perot interferometric sensors," IEEE Photon. Technol. Lett. **20**, 75 (2008).
90. Y. Jiang and C. Tang, "Fourier transform white-light interferometry based spatial frequency-division multiplexing of extrinsic Fabry–Perot interferometric sensors," Rev. Sci. Instrum. **79**, 106105 (2008).